

CHONDRULE FORMATION BY THE JOVIAN SWEEPING SECULAR RESONANCE

MUNAN GONG (龚慕南)¹, XIAOCHEN ZHENG (郑晓晨)², DOUGLAS N.C. LIN (林潮)^{2,3,4}, KEDRON SILSBEE¹, CLEMENT BARUTEAU⁵, SHUDE MAO (毛淑德)²

Accepted by ApJ

ABSTRACT

Chondrules are silicate spheroids found in meteorites, serving as important fossil records of the early solar system. In order to form chondrules, chondrule precursors must be heated to temperatures much higher than the typical conditions in the current asteroid belt. One proposed mechanism for chondrule heating is the passage through bow shocks of highly eccentric planetesimals in the protoplanetary disk in the early solar system. However, it is difficult for planetesimals to gain and maintain such high eccentricities. In this paper, we present a new scenario in which planetesimals in the asteroid belt region are excited to high eccentricities by the Jovian sweeping secular resonance in a depleting disk, leading to efficient formation of chondrules. We study the orbital evolution of planetesimals in the disk using semi-analytic models and numerical simulations. We investigate the dependence of eccentricity excitation on the planetesimal's size as well as the physical environment, and calculate the probability for chondrule formation. We find that 50 – 2000 km planetesimals can obtain eccentricities larger than 0.6 and cause effective chondrule heating. Most chondrules form in high velocity shocks, in low density gas, and in the inner disk. The fraction of chondrule precursors which become chondrules is about 4–9% between 1.5–3 AU. Our model implies that the disk depletion timescale is $\tau_{\text{dep}} \approx 1$ Myr, comparable to the age spread of chondrules; and that Jupiter formed before chondrules, no more than 0.7 Myr after the formation of the CAIs.

1. INTRODUCTION

Chondritic meteorites, or chondrites, contain some of the oldest and most primitive solids in our solar system. They record the physical conditions at the early phase of the solar nebula evolution and planet formation. Chondrites are mainly composed of chondrules, which are 0.1 to 1 millimeter sized silicate spheroids. The majority of chondrules formed 1 – 3 Myr after the calcium aluminum inclusions (CAIs), another component often found in chondrites and the oldest solids dated in the solar system (Scott 2007). To form the chondrules we see today, chondrule precursors need to be heated to temperatures above 1600 K and cooled down rapidly on timescales of minutes to hours (Desch et al. 2012). Considering ordinary chondrites make up $\sim 10\%$ of meteorites found on Earth (Desch et al. 2005), chondrule heating events should be common in the early solar system.

Many mechanisms have been proposed for chondrule heating, including solar flares (Shu et al. 2001), impacts between planetesimals (Urey & Craig 1953; Dullemond et al. 2014), and shock heating in the protoplanetary disk around the Sun (Iida et al. 2001; Ciesla & Hood 2002; Desch et al. 2005). Chondrule heating in planetesimals' bow shocks is one of the most promising models that can simultaneously explain many features in the thermal his-

tories of chondrules, such as the ambient temperature, the peak temperature, and the cooling rate (Desch et al. 2012). In recent years, detailed numerical simulations that model the structure of the bow shocks and the trajectories of chondrules confirmed that passing through the bow shocks of large planetesimals is a plausible mechanism for chondrule formation (Morris et al. 2012; Mann et al. 2016). However, there is one remaining puzzle in this model: in order to heat up chondrule precursors to the required high temperatures, the relative velocity between the planetesimal and the gas needs to be $v_{\text{rel}} \gtrsim 6$ km/s in relatively dense gas, and even higher if the gas density is lower (Iida et al. 2001; Mann et al. 2016). This is a significant fraction (24 – 37%) of the Keplerian speed in the asteroid belt region, and implies that the planetesimals responsible for chondrule heating need to be excited to high eccentricities.

One event that can lead to the eccentricity excitation of planetesimals is the formation of Jupiter. As the largest planet in the solar system, Jupiter can profoundly affect the dynamics of the planetesimals. With a thick gaseous atmosphere, Jupiter should have formed early, before the gas in the disk was significantly depleted. Weidenschilling et al. (1998) proposed that the strong 2:1 and 3:2 mean motion resonances with Jupiter can excite the eccentricities of planetesimals to $e_p \approx 0.3$. However, because the resonance locations are relatively far out in the disk (at 3.28 and 3.97 AU) where the Keplerian velocity is low ($\lesssim 16$ km/s), the planetesimals can only obtain velocities of $v_{\text{rel}} \lesssim 5$ km/s, not high enough for chondrule formation. Nagasawa et al. (2014) considered in addition the gravity of the disk which enables the secular resonance by Jupiter. They found that planetesimals at the location of resonance can gain $v_{\text{rel}} > 12$ km/s and lead to effective chondrule formation. However, they only considered a fixed disk mass and thus a fixed location of

¹ Max-Planck Institute for Extraterrestrial Physics, Garching by Munich, 85748, Germany; munan@mpe.mpg.de

² Department of Astronomy and Center for Astrophysics, Tsinghua University, Beijing 10086, China

³ Institute for Advanced Studies, Tsinghua University, Beijing 10086, China

⁴ Department of Astronomy and Astrophysics, University of California Santa Cruz, Santa Cruz, CA 95064, USA

⁵ Institut de Recherche en Astrophysique et Planétologie (IRAP) 14 avenue Edouard Belin, 31400 Toulouse, France

the Jovian secular resonance, and only planetesimals of a single size of 300 km.

In this paper, we investigate a scenario in which the orbits of planetesimals are influenced by both Jupiter and a depleting protoplanetary disk. As the disk mass decreases with time, the location of the Jovian secular resonance moves from the outer to the inner disk. This phenomenon is called the sweeping secular resonance, first proposed by Ward et al. (1976) to explain Mercury's large eccentricity and inclination.⁶ Subsequently, the sweeping secular resonance was invoked to explain other characteristics of the solar system, such as the formation and orbits of terrestrial planets (Nagasawa et al. 2005; Thommes et al. 2008), the mass deficit of the asteroid belt region in the minimum mass solar nebula (MMSN) model (Hayashi 1981; Zheng et al. 2017), and the size distribution of the asteroids (Zheng et al. 2017). We propose that the same mechanism can explain chondrule formation, by exciting the planetesimals in the asteroid belt region to high eccentricity orbits. We use both semi-analytic models and numerical simulations to investigate the dependence of eccentricity excitation on the planetesimal's size, as well as the environment and probability of chondrule formation.

The structure of this paper is as follows. Section 2 describes the method of our semi-analytic models and numerical simulations. In Section 3, we show our results on the orbital evolution of planetesimals, the size-dependent eccentricity excitation, and the chondrule formation probability and its dependence on the model parameters. In Section 4, we discuss the implications of chondrule formation on the formation of Jupiter and the depletion timescale of the disk. Finally, Section 5 summarises the main findings of this work.

2. METHODS

2.1. Semi-analytic Model

In this section, we describe our semi-analytic model for the eccentricity and semi-major axis evolution of planetesimals that are embedded in the protoplanetary disk and perturbed by the Jovian sweeping secular resonance. The secular perturbation by Jupiter excites the eccentricity of planetesimals, while gas drag damps both their eccentricities and semi-major axes. We assume the Sun, disk, planetesimals, and Jupiter are all in the same plane, and thus our model is 2-dimensional.

We consider the stage when Jupiter has already gained its present-day mass and opened a gap in the disk which quenched its accretion (Dobbs-Dixon et al. 2007). In this model, we assume that: (1) There is a thin, axisymmetric protoplanetary disk with power-law surface density distribution based on the MMSN model, with a gap near Jupiter's orbit (Bryden et al. 1999). The surface density of the disk depletes over time. (2) The masses of planetesimals are much smaller than the mass of Jupiter, and therefore, the gravitational perturbation by planetesimals on Jupiter is ignored. In our fiducial model, we do not consider the presence of Saturn, and Jupiter's semi-major axis and eccentricity are at their current day values ($a_J = 5.2$ AU, $e_J = 0.05$), and do not

evolve with time. The only time variation in Jupiter's orbit is its apsidal precession due to the gravity of the gas disk. (3) All planetesimals are initially embedded in the disk with circular orbits in the region of the present-day asteroid belt. Their subsequent orbital evolution is affected by the gravitational perturbation from Jupiter and the surrounding gas disk, as well as the gas drag from the disk.

Later, we introduce Saturn in some of our numerical simulations. Although Saturn introduces its own additional secular resonance and perturbs the orbit of Jupiter, we show that the excitation of planetesimals' eccentricities is still dominated by the Jovian sweeping secular resonance, and the chondrule formation probability is largely unchanged.

The physical picture of our model (without Saturn) is illustrated in Figure 1. We focus on the process of chondrule formation in this paper. Zheng et al. (2017) adopted a similar physical picture, but focused on the remaining distribution of planetesimals in the late stage after the gas disk is almost fully depleted.

Therefore, the equations for orbital evolution of Jupiter and the planetesimals can be written as:

$$\frac{de_p}{dt} = \frac{de_{p,J}}{dt} + \frac{de_{p,gas}}{dt} \quad (1)$$

$$\frac{d\xi}{dt} \equiv \frac{d(\varpi_p - \varpi_J)}{dt} = \frac{d\varpi_{p,J}}{dt} + \frac{d\varpi_{p,disk}}{dt} - \frac{d\varpi_{J,disk}}{dt} \quad (2)$$

$$\frac{da_p}{dt} = \frac{da_{p,gas}}{dt}, \quad (3)$$

where e_p , a_p and ϖ_p (e_J , a_J and ϖ_J) are the eccentricity, semi-major axis, and apsidal angle of the planetesimals (Jupiter). Given that the combined mass of planetesimals is much less than that of Jupiter, we can ignore the gravitational perturbation of planetesimals on Jupiter. In the sections below, we describe in detail the different terms in Equations (1), (2), and (3). These equations can be solved numerically as a set of coupled ordinary differential equations.

2.1.1. Sweeping Secular Resonance by Jupiter

The eccentricity vector of a planetesimal is modulated by the gravitational force from Jupiter. When $e_{p,J} \ll 1$, to the first order (Murray & Dermott 1999; Nagasawa et al. 2003):

$$\frac{de_{p,J}}{dt} = \frac{e_J}{t_p} C \sin \xi, \quad (4)$$

$$\frac{d\varpi_{p,J}}{dt} = \frac{1}{t_p} \left[\frac{e_J}{e_p} C \cos \xi + 1 \right]. \quad (5)$$

Here $C = -b_{3/2}^{(2)}(\alpha)/b_{3/2}^{(1)}(\alpha)$ and $t_p = [4/(n_p b_{3/2}^{(1)}(\alpha) \alpha^2)](M_\odot/M_J)$, where $n_p = \sqrt{GM_\odot/a_p^3}$ is the mean motion of the planetesimals, $\alpha \equiv a_p/a_J$ is the ratio of semi-major axes between the planetesimal and Jupiter, and $b_s^{(j)}$ are the Laplace coefficients.

The orbits of planetesimals and Jupiter precess due to the gravitational potential of the disk. We consider a thin disk with a power law surface density profile,

$$\Sigma(R) = f_g \Sigma_0 \left(\frac{R}{1\text{AU}} \right)^{-k}, \quad (6)$$

⁶ The sweeping secular resonance discussed in Ward et al. (1976) is caused by the decreasing oblateness of the Sun as its spin slows down, rather than the disk depletion as studied in this paper.

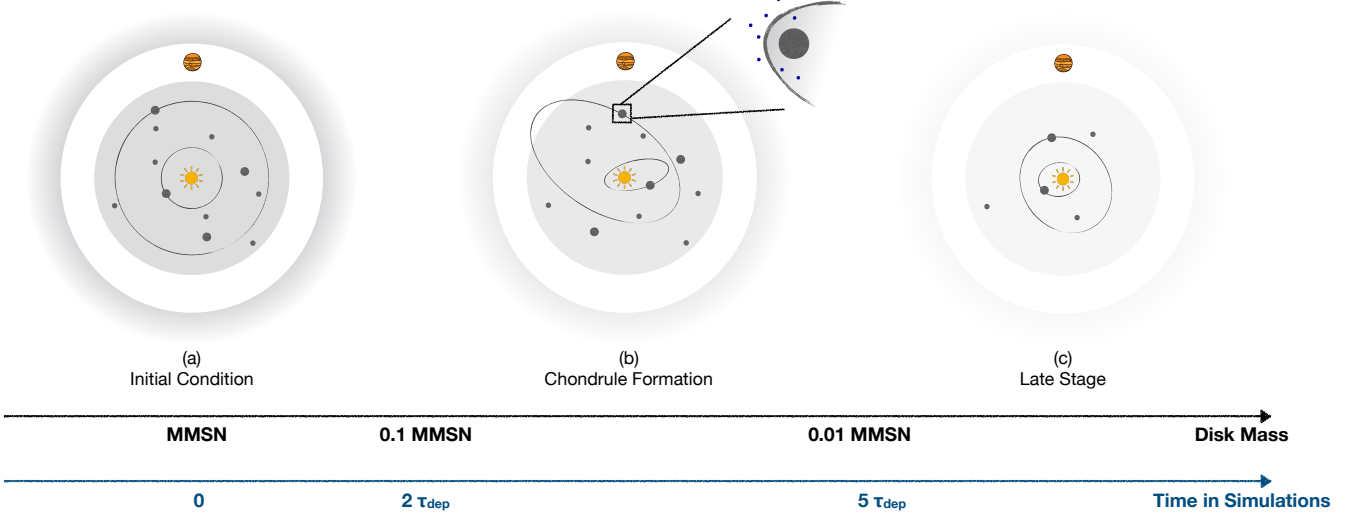


Figure 1. Schematic picture of our chondrule formation model. (a) Initial condition: Jupiter forms and opens a gap in the disk. The planetesimals are in circular orbits. (b) Chondrule formation: As the gas disk depletes over time, the sweeping secular resonance by Jupiter excites the eccentricities of planetesimals. Chondrules form in the bow shocks of highly eccentric planetesimals. (c) Late stage: The gas disk is almost fully depleted. Many planetesimals are ejected from the system by close encounters with Jupiter or removed from our simulation when they pass too close to the Sun. The remaining planetesimals are in orbits with moderate eccentricities.

where R is the radial coordinate. The initial disk surface density is set to match the MMSN model with $\Sigma_0 = 1700 \text{ g cm}^{-2}$ and $k = 3/2$ (Hayashi 1981). In order to mimic the depletion of the disk over time, we set the disk surface density to decay exponentially over timescale τ_{dep} :

$$f_g = \exp\left(-\frac{t}{\tau_{\text{dep}}}\right). \quad (7)$$

Observations of young clusters suggest that most stars lose their disk on a timescale of $\leq 3 \text{ Myr}$ (Zuckerman et al. 1995; Haisch et al. 2001). This idealized prescription for disk evolution does not take into account the possibility of interruption of gas accretion flow in the disk due to planets' tidal torque or photoevaporation at some critical radii. Nonetheless, it is useful to illustrate the consequence of gas depletion in the disk. We set the parameter $\tau_{\text{dep}} = 1 \text{ Myr}$ in our fiducial model, and explore the effect of varying τ_{dep} in Section 3.3.

The precession of Jupiter due to the disk with a power-law surface density profile (Equation (6)) and a gap surrounding Jupiter is given by (Ward 1981):

$$\begin{aligned} \frac{d\varpi_{J,\text{disk}}}{dt} &= \frac{2\pi G \Sigma(a_J)}{n_J a_J} \sum_{n=1}^{\infty} n(2n+1) A_n \\ &\times \left[\frac{(a_J/R_{\text{out}})^{2n-1+k}}{2n-1+k} + \frac{(R_{\text{in}}/a_J)^{2n+2-k}}{2n+2-k} \right] \\ &= \frac{d\varpi_{J,\text{disk}}}{dt} \Big|_{t=0} \exp\left(-\frac{t}{\tau_{\text{dep}}}\right), \end{aligned} \quad (8)$$

and the planetesimal precession rate due to the disk is given by

$$\begin{aligned} \frac{d\varpi_{p,\text{disk}}}{dt} &= \frac{2\pi G \Sigma(a_p)}{n_p a_p} \left(-\frac{1}{2} + \frac{S_k}{2} + S_{\text{out}} - S_{\text{in}} \right) \\ &= \frac{d\varpi_{p,\text{disk}}}{dt} \Big|_{t=0} \exp\left(-\frac{t}{\tau_{\text{dep}}}\right). \end{aligned} \quad (9)$$

Here R_{in} and R_{out} are the radii of the inner and outer edges of the gap, and $A_n = [(2n)!/(2^n n!)^2]^2$. We choose $R_{\text{in}} = 4.5 \text{ AU}$ and $R_{\text{out}} = 6 \text{ AU}$ based on numerical simulations by Bryden et al. (1999).⁷ In Equation (9), the constant term,

$$S_k = (k-1)(k-2) \sum_{n=1}^{\infty} A_n \frac{4n+1}{(2n-1+k)(2n+2-k)}, \quad (10)$$

and $S_k = -0.094$ for $k = 3/2$. The other two terms, S_{out} and S_{in} , are from the inner and outer edges of the gap,

$$S_{\text{out}} = \sum_{n=1}^{\infty} n(2n+1) A_n \frac{(a_p/R_{\text{out}})^{2n-1+k}}{2n-1+k}, \quad (11)$$

$$S_{\text{in}} = \sum_{n=1}^{\infty} n(2n+1) A_n \frac{(a_p/R_{\text{in}})^{2n-1+k}}{2n-1+k}. \quad (12)$$

The secular resonance between a planetesimal and Jupiter occurs when their apsidal precession rates coincide, leading to the growth of the planetesimal's eccentricity. The location of Jovian resonance ν_5 can be solved analytically: setting $d\xi/dt = 0$ in Equation (2) and combining with Equations (8) and (9), the time t when resonance occur at a radius R is given by

$$\frac{t}{\tau_{\text{dep}}} = -\ln \left(\frac{\frac{d\varpi_{p,J}}{dt}}{\frac{d\varpi_{J,\text{disk}}}{dt} \Big|_{t=0} - \frac{d\varpi_{p,\text{disk}}}{dt} \Big|_{t=0}} \right), \quad (13)$$

where the numerator is evaluated at time $t = 0$. The location of ν_5 as a function of time is shown in Figure 2. As the disk surface density depletes over time, ν_5 moves closer to the Sun. The gap carved by Jupiter delays the time when ν_5 passes a particular location: at $t \lesssim \tau_{\text{dep}}$,

⁷ We use the results from their model 1B with the disk scale-height $H/R = 0.04$ and the turbulent viscosity parameter $\alpha = 0.001$ (Shakura & Sunyaev 1973). More recent simulations by Dürmann & Kley (2015) also obtained similar results.

there is no resonance inside ~ 4 AU. Jupiter's secular resonance only starts to stir up the planetesimals after the disk is significantly depleted.

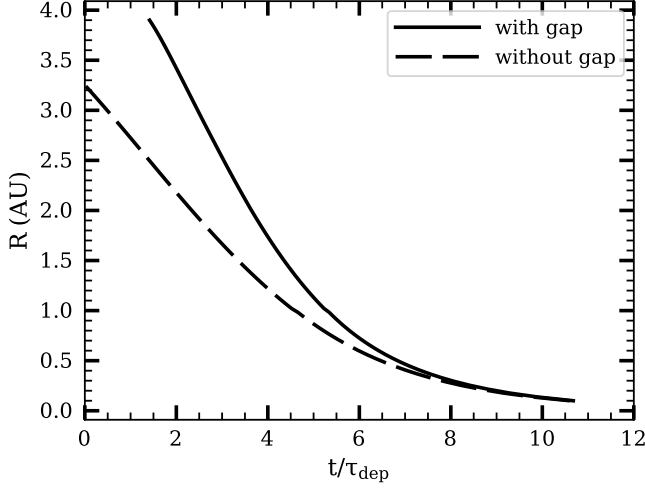


Figure 2. Location of Jupiter's secular resonance ν_5 with a gap in the disk between 4.5–6 AU (solid) and without a gap (dashed).

2.1.2. Damping by the Gas Disk

The gas in the disk damps the eccentricity and semi-major axis of a planetesimal through aerodynamic and tidal effects. We follow Zhou & Lin (2007) to estimate the gas drag. The formulae only include the lowest order terms assuming $e_p, \eta \ll 1$ (η is a parameter related to the pressure gradient, see Equation (23)).

The acceleration of a planetesimal with mass m_p and radius r_p by aerodynamic drag is

$$\mathbf{f}_{\text{aero}} = -\frac{1}{2m_p} C_D \rho_g \pi r_p^2 |\mathbf{v}_{\text{rel}}| \mathbf{v}_{\text{rel}}, \quad (14)$$

where $C_D = 0.44$ is the coefficient for objects with large Reynolds number (Whipple 1972), ρ_g is the gas density, and $\mathbf{v}_{\text{rel}} = \mathbf{v}_{\mathbf{k}} - \mathbf{v}_{\mathbf{g}}$ is the relative velocity between the Keplerian motion of the planetesimal ($\mathbf{v}_{\mathbf{k}}$) and the sub-Keplerian velocity of the gas ($\mathbf{v}_{\mathbf{g}}$) due to pressure gradients in the disk. Because planetesimals are expected to settle near the disk mid-plane, we use the gas density at the mid-plane for calculating the aerodynamic drag. The disk vertical (\hat{z}) structure is set by the balance between gas pressure and gravity, giving

$$\rho_g(R, z) = \rho_g(R, 0) \exp\left(-\frac{z^2}{2H^2}\right), \quad (15)$$

where the disk scale height $H = c_s/\Omega_k$, $c_s = \sqrt{k_B T / \mu m_H}$ is the sound speed and $\Omega_k = \sqrt{GM_\odot / R^3}$ is the Keplerian angular velocity, m_H is the proton mass, and k_B is the Boltzmann constant. The mean molecular weight of the gas $\mu = 7/3$, assuming the disk to be made up of H_2 and He with the solar abundance $n(\text{H}_2) : n(\text{He}) = 5 : 1$. We adopt the temperature profile of the disk in the MMSN model (Hayashi 1981):

$$T = T_0 \left(\frac{R}{1\text{AU}}\right)^{-1/2} = 280 \text{ K} \left(\frac{R}{1\text{AU}}\right)^{-1/2}, \quad (16)$$

which gives the disk scale-height

$$\frac{H}{R} = 0.033 \left(\frac{R}{1\text{AU}}\right)^{1/4} \left(\frac{T_0}{280\text{K}}\right)^{1/2}, \quad (17)$$

and gas density at the mid-plane

$$\begin{aligned} \rho_g(R, 0) &= \frac{\Sigma}{\sqrt{2\pi}H} = 1.36 \times 10^{-9} \text{ g cm}^{-3} \\ &\times f_g \left(\frac{R}{1\text{AU}}\right)^{-11/4} \left(\frac{T_0}{280\text{K}}\right)^{-1/2}. \end{aligned} \quad (18)$$

The effect of aerodynamic gas drag on the secular evolution of a planetesimal's orbit is derived by Adachi et al. (1976) (to the lowest order in e_p and η), assuming the gas in the disk follows circular orbits:

$$\frac{1}{a_p} \left(\frac{da_p}{dt}\right)_{\text{aero}} = -\frac{2}{\tau_{\text{aero}}} \left(\frac{5}{8}e_p^2 + \eta^2\right)^{1/2} (e_p^2 + \eta) \quad (19)$$

$$\frac{1}{e_p} \left(\frac{de_p}{dt}\right)_{\text{aero}} = -\frac{1}{\tau_{\text{aero}}} \left(\frac{5}{8}e_p^2 + \eta^2\right)^{1/2}, \quad (20)$$

where τ_{aero} is the aerodynamic drag timescale given by

$$\begin{aligned} \tau_{\text{aero}} &= \frac{2m_p}{\pi C_D r_p^2 \rho_g v_k} \\ &= \frac{4.75}{f_g} \text{yr} \left(\frac{R}{1\text{AU}}\right)^{13/4} \left(\frac{r_p}{1\text{km}}\right) \left(\frac{\rho_p}{1\text{g/cm}^3}\right) \left(\frac{T_0}{280\text{K}}\right)^{1/2}, \end{aligned} \quad (21)$$

η is a parameter related to the radial pressure gradient in the disk

$$\eta(R) = \frac{13}{8} \left(\frac{H}{R}\right)^2 = 1.5 \times 10^{-3} \left(\frac{R}{1\text{AU}}\right)^{1/2} \left(\frac{T_0}{280\text{K}}\right), \quad (23)$$

and v_k the Keplerian velocity of a circular orbit $v_k = \sqrt{GM_\odot/R}$.

The densities of planetesimals are expected to be in the range of $\sim 1 - 5.5 \text{ g cm}^{-3}$. Small planetesimals may be considered as pebble/ice piles, while large planetesimals may have gone through differentiation processes, similar to iron/stone meteorites. We use a simple prescription for the densities of planetesimals, following Zheng et al. (2017):

$$\rho_p(r_p) = \begin{cases} 1.0 \text{ g cm}^{-3}, & r_p \leq 18\text{km}, \\ \frac{r_p}{18\text{km}} \text{ g cm}^{-3}, & 18\text{km} < r_p < 100\text{km}, \\ 50/9 \text{ g cm}^{-3}, & r_p \geq 100\text{km}. \end{cases} \quad (24)$$

In addition to the aerodynamic drag, large planetesimals also experience the tidal drag force by the disk through Lindblad resonances (Ward 1988; Artymowicz 1993; Thommes et al. 2008). The typical timescale for

tidal damping by Lindblad torque is given by

$$\begin{aligned}\tau_{\text{tidal}} &= \left(\frac{m_p}{M_\odot}\right)^{-1} \left(\frac{\Sigma R^2}{M_\odot}\right)^{-1} \left(\frac{c_s}{v_k}\right)^4 \Omega_k^{-1} \\ &= \frac{4.92 \times 10^5 \text{ yr}}{f_g} \\ &\times \left(\frac{\rho_p}{1 \text{ g/cm}^3}\right)^{-1} \left(\frac{r_p}{10^3 \text{ km}}\right)^{-3} \left(\frac{R}{1 \text{ AU}}\right)^2 \left(\frac{T_0}{280 \text{ K}}\right)^2.\end{aligned}\quad (25)$$

In addition to the Lindblad resonances, the corotation torques also contribute to the drag force (Paardekooper et al. 2011). With the disk profile adopted in this work, the corotation torque is small compared to the Lindblad torque for circular orbits (Paardekooper et al. 2011). Furthermore, numerical simulations in Fendyke & Nelson (2014) show that corotation torque decreases with increasing eccentricity. Therefore, we neglect the corotation torque in our models.

Numerical simulations of the orbital evolution of planetesimals in a gaseous disk obtained a tidal damping timescale similar to the analytic expression in Equation (25) for planetesimals with low eccentricities (Papaloizou & Larwood 2000), and different tidal damping timescales depending on the disk structure for highly-eccentric planetesimals (Muto et al. 2011). However, the results from these 2-dimensional numerical simulations depend sensitively on the numerical softening parameter, which is uncertain and arbitrary. Therefore, we choose to use the simple analytic expression in Equation (25). To investigate the dependence of our results on the tidal damping, we run an additional numerical simulation (TDL5 in Table 1) with five times stronger tidal damping (multiplying τ_{tidal} in Equation (25) by a factor of 0.2).

The acceleration of a planetesimal due to the tidal drag force can be estimated using the formulation in Komiya & Ida (2002),

$$\mathbf{f}_{\text{tidal}} = -\frac{\mathbf{v}_{\text{rel}}}{\tau_{\text{tidal}}}.\quad (26)$$

Similar to the aerodynamic drag, the secular evolution of a planetesimal’s orbital elements due to the tidal drag is given by Adachi et al. (1976) (their Equation (4.18)):⁸

$$\frac{1}{a_p} \left(\frac{da_p}{dt}\right)_{\text{tidal}} = -\frac{2}{\tau_{\text{tidal}}} \left(\eta + \frac{13}{16} e_p^2\right),\quad (27)$$

$$\frac{1}{e_p} \left(\frac{de_p}{dt}\right)_{\text{tidal}} = -\frac{1}{\tau_{\text{tidal}}}.\quad (28)$$

Figure 3 shows the aerodynamic and tidal damping timescales for planetesimals with $a_p = 2.5 \text{ AU}$ and sizes ranging from 0.1 to 10^4 km , as described by Equations (19), (20), (27) and (28). When the size of a planetesimal increases, the aerodynamic timescale increases whereas the tidal timescale decreases. We can roughly divide the planetesimals into three groups according to the gas-damping that they experience: planetesimals with

$r_p \lesssim 50 \text{ km}$ are subject to “strong aerodynamic damping”, $r_p \sim 50 - 2000 \text{ km}$ are “weakly coupled” to the gas, and $r_p \gtrsim 2000 \text{ km}$ are subject to “strong tidal damping”. Planetesimals in these different groups have very different behavior, which we discuss in detail in Section 3.1. The planetesimals in the “weakly coupled” group are less susceptible to the damping of their eccentricity by gas drag, and can easily obtain high eccentricities by gravitational interaction with Jupiter.

2.2. Numerical Simulation

The analytic model in Section 2.1 is based on two key assumptions. First, Jupiter only affects the orbits of planetesimals by secular gravitational perturbations. Other gravitational effects by Jupiter, such as the mean motion resonance, are ignored. Second, the formulations for the orbital evolution of planetesimals are obtained by using linear perturbation theory, which breaks down when the eccentricities of planetesimals are of order unity.

To test these assumptions and to obtain a more complete picture of the orbital evolution of planetesimals, we carry out numerical simulations using a modified version of the publicly available N-body code *HERMIT4* (Aarseth 2003). The simulation setup in our fiducial model is very similar to the model A_5 in Zheng et al. (2017). We briefly summarize the method of our simulations here, and refer the readers to Zheng et al. (2017) for more details.

The N-body code computes the gravitational interactions between the Sun and Jupiter, and the gravitational forces from the Sun and Jupiter to the planetesimals. We ignore the gravitational interaction from the planetesimals back to the Sun and Jupiter, and between the planetesimals themselves. Jupiter and the planetesimals also feel the gravitational potential from the disk, which leads to precession of their orbits. The gas drag is calculated by adding drag forces to the planetesimals’ equations of motion, as described in Equations (14) and (26).

We place the planetesimals initially in circular orbits with random phase angle between 0 and 2π . We put 2000 planetesimals with semi-major axes drawn from a random distribution between 1.5 and 3.5 AU. The sizes of the planetesimals are randomly drawn from a flat distribution in logarithm space between 10 and 5000 km. Later, when we calculate the chondrule formation probability, we scale the number of planetesimals in each size bin to fit the realistic size distributions of planetesimals (see Section 3.3).

We ran the simulation for 10 times the disk depletion time. Because we are interested in planetesimals that pass the main belt region of $R = 1.5 - 3.5 \text{ AU}$, we stop tracking a planetesimal once its semi-major axis is smaller than 0.7 AU or larger than 7 AU. For numerical reasons, we also remove planetesimals that come within 0.07 AU of the Sun.

In order to investigate the effects of our assumptions and parameters on chondrule formation, we run a series of numerical models with different setups, as summarized in Table 1. We explore different values of the disk depletion time, tidal damping strength, and the initial eccentricity of Jupiter. We also add Saturn in two models, with its semi-major axis at its current day value or at 3 : 2 mean motion resonance with Jupiter. In models

⁸ In the limit of circular orbits, Equation (27) does not recover the typical formulae for type I migration (e.g. Paardekooper et al. 2011; Baruteau et al. 2014). However, here we focus on the semi-major axis and eccentricity damping of planetesimals with high eccentricities.

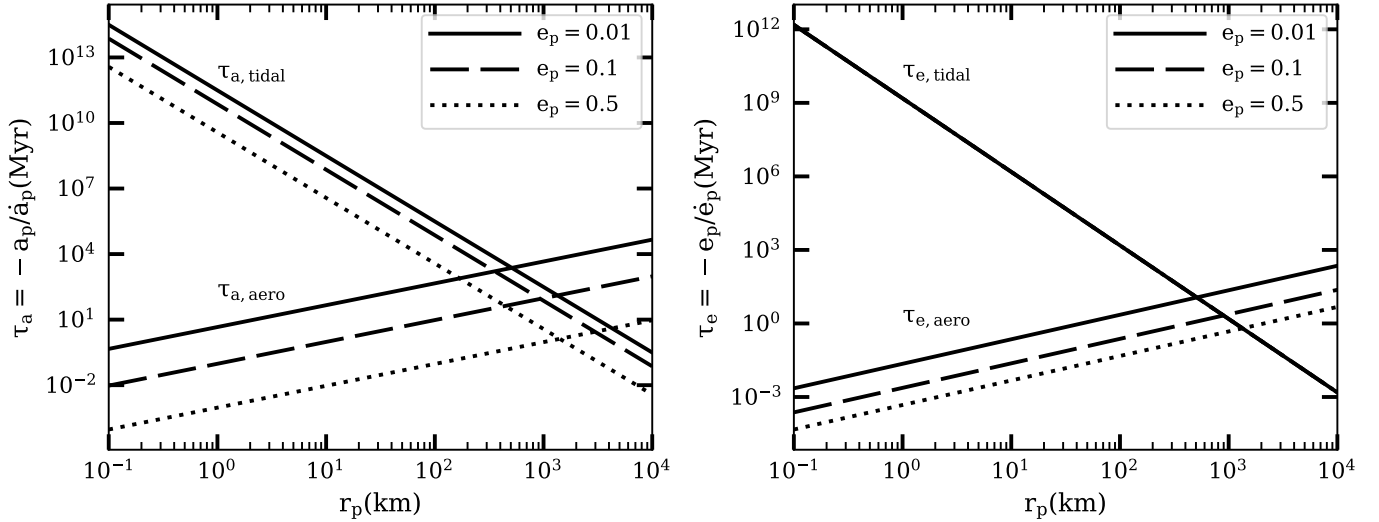


Figure 3. Timescales for semi-major axis decay $\tau_a = -a_p/\dot{a}_p$ (left panel) and eccentricity decay $\tau_e = -e_p/\dot{e}_p$ (right panel) of planetesimals with radius $r_p = 0.1 - 10^4$ km by aerodynamic or tidal gas drag. The planetesimals have semi-major axes $a_p = 2.5$ AU. The solid, dashed and dotted lines show the cases in which the eccentricities of the planetesimals are $e_p = 0.01, 0.1$ and 0.5 .

with Saturn, the gap is larger, encompassing the orbits of both Jupiter and Saturn. Saturn interacts gravitationally with the Sun, planetesimals, and the gas disk in the same way as Jupiter. The gravitational interaction between Saturn and Jupiter is also included. The initial semi-major axis of Jupiter is always at its current day value ($a_J = 5.2$ AU).

Table 1
Parameters for the Numerical Simulations

model ID	τ_{dep} (Myr)	$e_{J,0}^a$	gap (AU) ^b	$a_{S,0}$ (AU) ^c
fiducial	1	0.05	4.5–6	-
DEP0p5	0.5	0.05	4.5–6	-
DEP2	2	0.05	4.5–6	-
TDL5 ^d	1	0.05	4.5–6	-
EJ0p1	1	0.1	4.5–6	-
ST	1	0.05	4.5–11	9.58
STR	1	0.05	4.5–11	6.81

^aThe initial eccentricity of Jupiter.

^bThe inner and outer radii of the gap opened by Jupiter (and Saturn, if it is in the model) in the gaseous disk.

^cThe initial semi-major axis of Saturn. “-” denotes that Saturn is not included in the model. Saturn’s initial semi-major axis is at its current day value in model ST. In model STR, Saturn and Jupiter are in 3:2 mean-motion resonance, and we reduce Saturn’s semi-major axis accordingly.

^dIn model TDL5, we increase the strength of tidal damping by a factor of 5 (multiplying τ_{tidal} in Equation (25) by a factor of 0.2). All other parameters are the same as the fiducial model.

2.3. Probability of Chondrule Formation

In order for chondrules to form in the bow shock of a planetesimal, the relative velocity v_{rel} between the planetesimal and the gas has to be in a certain range: the velocity needs to be high enough to melt chondrule precursors and low enough to avoid complete evaporation. We use the result from Iida et al. (2001) (their Equations (37) and (38)) for the velocity range required for chondrule formation. This velocity range depends on gas density, which affects the heating rate of chondrule precursors.

We use the following method to estimate the probability of chondrule formation. For each planetesimal, the mass of chondrule precursors going through the shock region per unit time is

$$\frac{dM_{c,\text{heating}}}{dt} = \sigma_c v_{\text{rel}} n_c m_c, \quad (29)$$

where σ_c is the cross-section of the shock region, v_{rel} is the relative velocity between the planetesimal and the chondrule precursors, n_c is the number density of chondrule precursors, and m_c is the mass of a single chondrule precursor. The stopping time for chondrule precursors can be estimated from the Epstein gas drag law (Epstein 1924)

$$t_s = \frac{\rho_d a_d}{\rho_g c_s}, \quad (30)$$

where ρ_d and a_d are the material density and radius of the chondrule precursor. t_s increases over time as the gas depletes and ρ_g drops in our disk model. For the time range of chondrule formation (Figure 7), t_s of mm-sized particles in the disk mid-plane within 3.5 AU is less than 1% of the orbital time. Therefore it is safe to assume that the chondrule precursors are well-coupled with the gas, and v_{rel} is simply the relative velocity between the planetesimal and the gas. Morris et al. (2012) simulated the bow shocks from $r_p > 500$ km planetesimals, and found that the cross-section of the shock region is roughly proportional to the geometric cross-section $\sigma_c \approx \pi(1.6r_p)^2$. For smaller planetesimals, the gravitational focusing from the planetesimals is weaker and their atmosphere is thinner, and σ_c approaches the geometric cross-section πr_p^2 . Since the exact dependence of σ_c on r_p is unknown, we adopt $\sigma_c = \pi(1.6r_p)^2$ for planetesimals of all sizes in our simulations for simplicity. We assume that the chondrule precursors are distributed in a dust disk with a similar profile as the gas disk (Equation (15)), $\rho_c(R, z) = \rho_c(R, 0) \exp(-z^2/2H_c^2)$. Σ_c is the surface density of chondrule precursors and follows the same scaling with radius as the MMSN, $\Sigma_c \propto R^{-1.5}$. H_c is the scale height of the chondrule precursors from the disk

mid-plane. We assume the planetesimals to be confined near the mid-plane of the disk, and use the mid-plane density of the chondrule precursors $\rho_c = \Sigma_c / (\sqrt{2\pi} H_c)$ in Equation (29). Due to gas drag and the gravity from the central star, dust grains settle down toward the disk mid-plane and thus have a smaller scale height than the gas disk. The dust disk scale-height depends both on the grain size which determines the gas drag, and the turbulence level in the disk which affects how efficiently grains can be lifted away from the mid-plane. We adopt the dust disk scale-height H_c from numerical simulations of turbulent disk with magnetic fields and ambipolar diffusion by Xu et al. (2017):

$$H_c = \sqrt{\frac{\alpha_z}{\tau_s}} H, \quad (31)$$

where $\alpha_z = 7.8 \times 10^{-4}$ is the vertical turbulence diffusion coefficient, and H the gas disk scale-height.⁹ $\tau_s = \Omega_k t_s$ is the dimensionless stopping time. As the disk depletes over time, the gas density ρ_g drops, leading to larger τ_s and smaller H_c . We choose $\rho_d = 1 \text{ g/cm}^3$ and $a_d = 1 \text{ mm}$ for the chondrule precursors, which gives $H_c/H = 0.2 - 0.9$ between $1.5 - 3.0 \text{ AU}$ and $t/\tau_{\text{dep}} = 2.5 - 4.5$.

Let P_c be the average probability that a particular dust grain between disk radius R_1 and R_2 becomes a chondrule. Then the contribution to P_c from a planetesimal between R_1 and R_2 is given by

$$\begin{aligned} \frac{dP_c}{dt} &= \frac{1}{M_{c,\text{tot}}} \frac{dM_{c,\text{heating}}}{dt} = \frac{\sigma_c v_{\text{rel}} \Sigma_c(R) / (\sqrt{2\pi} H_c(R))}{\int_{R_1}^{R_2} \Sigma_c(R') 2\pi R' dR'} \\ &= \frac{\sigma_c v_{\text{rel}} R^{-3/2}}{4\pi \sqrt{2\pi} H_c (R_2^{1/2} - R_1^{1/2})}, \end{aligned} \quad (32)$$

where $M_{c,\text{tot}}$ is the total mass of chondrule precursors. We choose the chondrule forming region to be between $R_2 = 3.0 \text{ AU}$ and $R_1 = 1.5 \text{ AU}$.

The contribution to P_c from one planetesimal is calculated by integrating Equation (32) over the time period when v_{rel} is in the suitable range for chondrule heating. With many planetesimals in our simulations, we can then estimate the average contribution to P_c from planetesimals of different sizes that satisfy the chondrule formation criteria, as well as the distribution of P_c over physical parameters such as time, relative velocity, gas density, and radial locations in the disk. We adopt the size distribution of planetesimals from collisional evolution simulations by Walsh & Levison (2019, hereafter WL2019). In their simulation, planetesimals in the inner disk grow faster than in the outer disk due to the higher surface density of solids. Because the first chondrules formed about 1 Myr after the CAIs (Scott 2007), we use the simulated size distribution of planetesimals from WL2019 at 1 Myr, as shown in Figure 4. In their simulations, the planetesimals located beyond 1.5 AU have

not had enough time to reach the runaway or oligarchic growth stage at 1 Myr due to collisional fragmentation. To investigate the dependence of chondrule formation on the size distribution of planetesimals, we also adopt a standard power-law size distribution of the planetesimals for $r_p = 10 - 2000 \text{ km}$, $dN/dr_p \propto r_p^{-3.5}$ (Mathis et al. 1977, hereafter MRN) for comparison. As shown in Section 3.2, planetesimals with $r_p \gtrsim 2000 \text{ km}$ do not make a significant contribution to chondrule heating due to the strong tidal force from the gas disk. The surface density of the planetesimals is assumed to be 1% of the initial surface density of the gas disk.

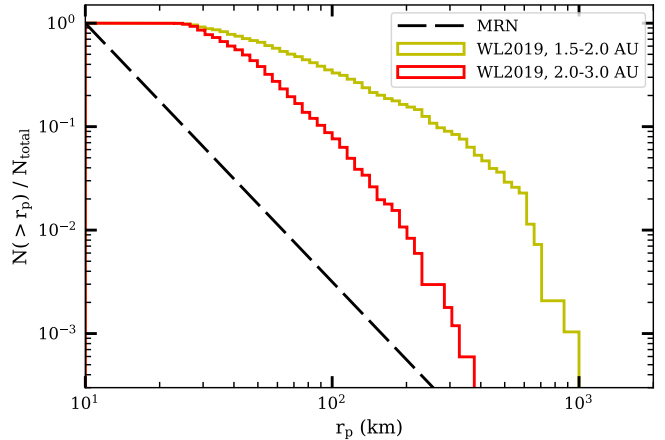


Figure 4. The cumulative size distribution of planetesimals from the collisional growth simulations by WL2019 at 1 Myr in different disk radius ranges (see legends), and the standard MRN size distribution of $dN/dr_p \propto r_p^{-3.5}$ (Mathis et al. 1977). In the MRN distribution, we set the largest planetesimal size to be $r_p = 2000 \text{ km}$. In WL2019, the largest planetesimal beyond 1.5 AU has grown to $r_p \approx 1000 \text{ km}$ at 1 Myr.

3. RESULTS

3.1. Orbital Evolution of Planetesimals

The time-evolution of the semimajor-axis and eccentricity of individual planetesimals in the fiducial model is shown in Figure 5. The sizes of planetesimals are selected to represent different regimes of gas-damping (see Section 2.1.2): $r_p = 10 \text{ km}$ represents the “strong aerodynamic damping” group, $r_p = 100 \text{ km}$ and $r_p = 1000 \text{ km}$ the “weakly coupled” group, and $r_p = 2000 \text{ km}$ the “strong tidal damping” group. Planetesimals in each group show distinctively different behaviors.

Before we delve into the details of the orbital evolution of planetesimals, it is helpful to understand the comparison between the semi-analytic results and numerical simulations. There are two major differences. First, the mean-motion resonances are not included in the semi-analytic calculations. The 2:1 mean-motion resonance with Jupiter at 3.3 AU is especially powerful in eccentricity excitation of planetesimals. The 2:1 resonance also has a large width, which depends on the eccentricity of the planetesimal, and is very wide at low eccentricity (see Murray & Dermott (1999) Chapter 8.7). The planetesimals with initial semi-major axes at 3.5 AU start within the width of 2:1 resonance. Their eccentricities increase, leading to the inward migration by gas drag which brings them closer to the 2:1 resonance, result-

⁹ The simulations in Xu et al. (2017) adopt an ambipolar diffusion Elsasser number $Am = 1$, which is more suitable for the outer disk $\gtrsim 30 \text{ AU}$. In the inner disk where chondrules form, the ambipolar diffusion and other non-ideal MHD effects are likely to be stronger, and therefore the turbulence in the disk is likely to be even weaker. This will lead to a smaller H_c and a higher chondrule formation efficiency.

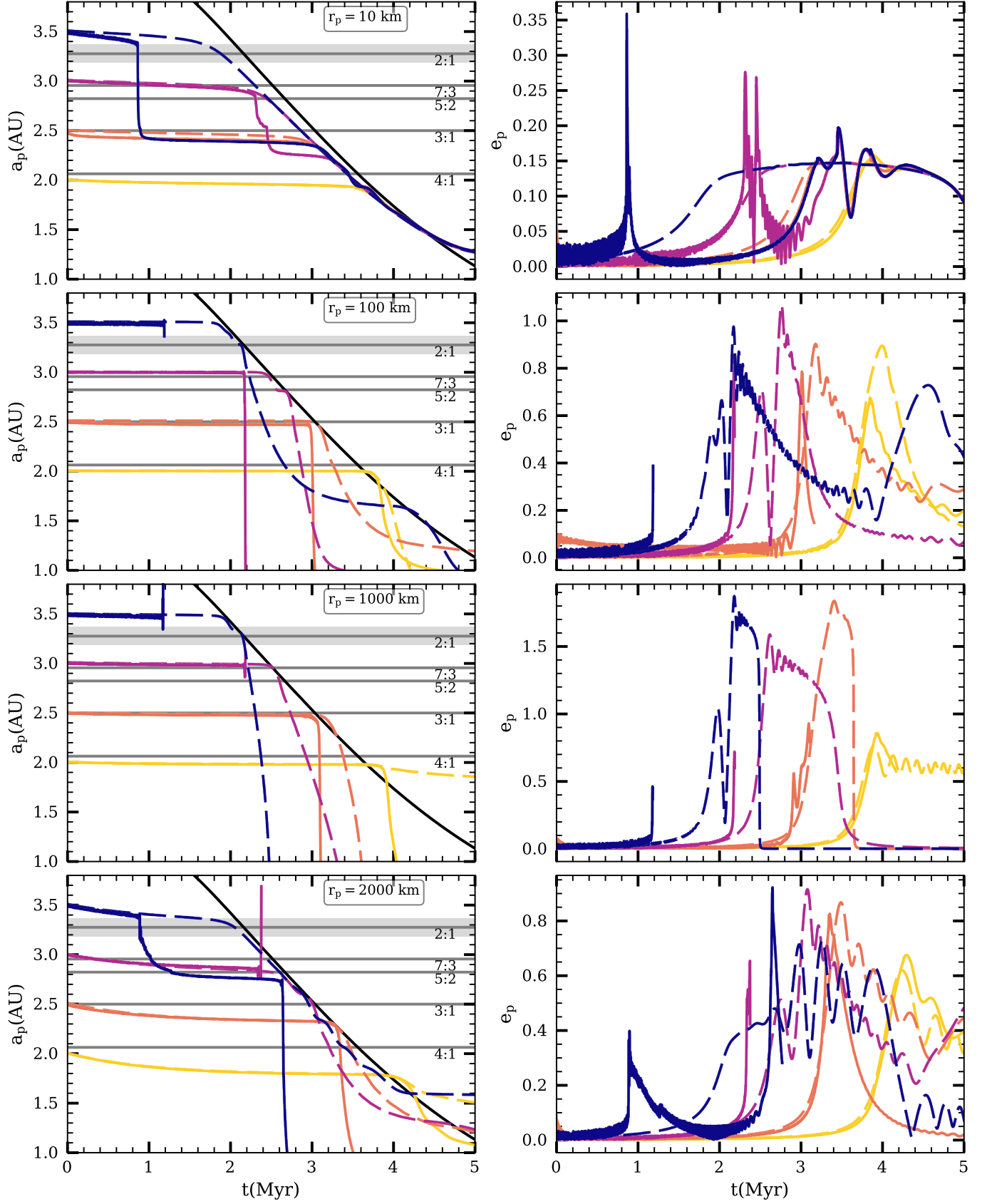


Figure 5. Semi-major axis (left) and eccentricity (right) evolution of planetesimals with radius from 10 to 2000 km (top to bottom). The black solid lines in the left panels show the location of the ν_5 resonance, same as the black solid line in Figure 2. Dashed and solid lines show the results from semi-analytic estimation and numerical simulations. Different colors represent planetesimals with different initial semi-major axes $a_{p,0} = 2.0, 2.5, 3.0$ and 3.5 AU (see left panels at $t = 0$). The horizontal grey lines mark the locations of mean motion resonances. The grey shaded region indicates the width of the 2:1 mean motion resonance for a planetesimal with $e_p = 0.2$.

ing in even stronger eccentricity excitation. As a result, many of them gain very large eccentricities, and some are ejected from the system by close encounters with Jupiter. Similarly, planetesimals with initial semi-major axes at 3.0 AU are also influenced by the 7:3, 5:2 and 3:1 resonances, although these resonances are weaker than the 2:1 resonance. Second, because our semi-analytic treatment of the secular resonance is only valid to the first order in eccentricity, it is no longer a good approximation when e_p is close to unity. For example, planetesimals with $a_{p,0} = 2.0$ AU in Figure 5 (yellow lines) are not strongly affected by the mean motion resonances, and the semi-analytic models and numerical simulations agree well when $e_p \lesssim 0.5$, confirming that the numerical simulations correctly capture the secular resonance. At $e_p \gtrsim 0.5$, the semi-analytic solutions deviate from the numerical simulations due to the failure of the first-order approximation.

The orbital evolution of the 10 km-sized planetesimals is shown in the top panels of Figure 5. Planetesimals with $a_{p,0} = 3.0$ AU and 3.5 AU are excited to moderate eccentricities $e_p \sim 0.3$ by mean-motion resonance and quickly migrate inward due to the strong aerodynamic gas drag. When caught in the secular resonance, they can “surf” with the resonance: they maintain small eccentricities $e_p \sim 0.2$, which allow them to migrate inward along with the ν_5 .

Planetesimals with sizes $r_p = 100$ and 1000 km experience much weaker gas drag (middle panels of Figure 5). As a result, their eccentricities can be easily excited to high values close to unity. Note that the eccentricity is not limited to be below unity in the semi-analytic calculations, but the first order approximation is also no longer valid in this case. Most of the planetesimals quickly leave the simulation domain either by rapid inward migration or close-encounter with Jupiter. As will be discussed in Section 3.3, chondrules can be heated efficiently in the bow shock of this “weakly coupled” group of planetesimals.

Very large planetesimals with $r_p \gtrsim 2000$ km are affected by strong tidal damping (lower panels of Figure 5). Unlike the aerodynamic drag, tidal drag can cause inward migration even when the planetesimal is in a circular orbit. This can be seen from Equations (19) and (27): for a circular orbit ($e_p = 0$), the timescale for inward-migration due to aerodynamic drag is proportional to η^2 but the timescale for tidal drag is proportional to η . The inward migration of 2000 km planetesimals causes them to encounter the secular resonance later at smaller disk radii. Planetesimals with $r_p \gtrsim 4000$ km migrate inward so rapidly that they never encounter the sweeping secular resonance (see Figure 6 and discussion).

3.2. Size-dependent Eccentricity Excitation

To summarise the size-dependent eccentricity excitation of planetesimals, we plot the maximum eccentricity of each planetesimal versus its size in the fiducial model in Figure 6. The semi-analytic models and numerical simulations give similar results, except for very high eccentricities $e_p \gtrsim 0.5$ when the semi-analytic approximation is no longer valid, and for planetesimals with initial semi-major axes $a_{p,0} \geq 3$ AU (blue and purple symbols) that are strongly affected by mean-motion resonances. At a fixed r_p and $a_{p,0}$, the spread of the $e_{p,\max}$ in numer-

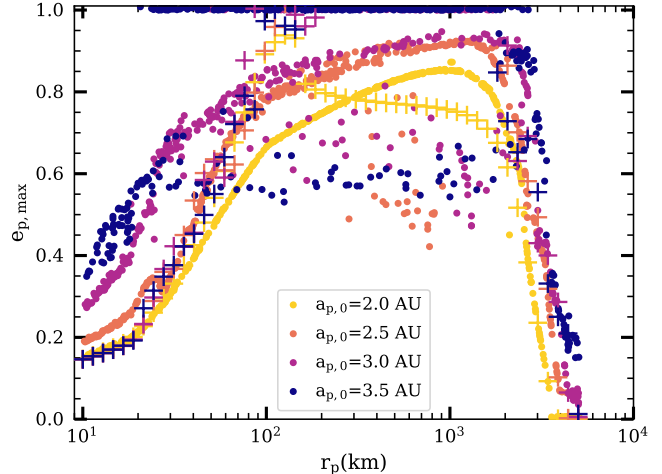


Figure 6. Maximum eccentricities versus radii of planetesimals for semi-analytic models (crosses) and numerical simulations (circles). Each dot represents one planetesimal. Different colors represent planetesimals with different initial semi-major axes $a_{p,0} = 2.0, 2.5, 3.0$ and 3.5 AU (same as Figure 5, see also the legend). The dots with $e_p = 1$ represent planetesimals that are ejected from the system.

ical simulations is caused by the random initial phase angles. In the “strongly coupled” group of small and large planetesimals, the spread of $e_{p,\max}$ is small at a given $a_{p,0}$, showing that their orbital evolution is not sensitive to the initial phase angle. In the “weakly coupled” group of intermediate size planetesimals, most of the planetesimals are still in the main distribution of $e_{p,\max}$ as a function of r_p . However, there are some outliers that have lower eccentricity $e_p \sim 0.6$ or extremely high eccentricity $e_p \sim 1$. These outliers are planetesimals that have close encounters with Jupiter, and planetesimals that pass through the ν_5 resonance with less eccentricity excitation or inward migration. Zheng et al. (2017) discusses this in more details (see their Figure 9).

The dependence of the planetesimal’s maximum eccentricity on its size exhibits the behavior one would expect from the gas drag laws discussed in Section 2.1.2. As the size increases, the maximum eccentricity $e_{p,\max}$ first increases due to decreased aerodynamic drag and then decreases again due to increased tidal drag. Because the aerodynamic damping timescale is proportional to r_p and the tidal damping timescale is proportional to r_p^{-3} (Equations (21) and (25)), the drop of $e_{p,\max}$ is steeper at large r_p . Very large planetesimals with $r_p \gtrsim 4000$ km migrate inward rapidly due to the tidal drag, and never encounter the secular resonance. Planetesimals with $r_p \approx 50 - 2000$ km can be excited to very high eccentricities $e_p > 0.7$ and are the primary contributors to chondrule formation.

3.3. Probability of Chondrule Formation

3.3.1. Overall Behavior

The total chondrule formation probability and the age spread of chondrules in different numerical models are summarized in Table 2. The age spread of chondrules is $\sim 1 - 2$ times the disk depletion time τ_{dep} in all of our models. This is because most chondrules form when the secular resonance sweeps through the main asteroid belt region, which happens on a timescale comparable to the disk depletion time. The total chondrule forma-

Table 2
Chondrule Formation Probability and Age Spread^a

model ID	WL2019		MRN	
	$P_{c,tot}$	$\Delta t/\tau_{dep}$	$P_{c,tot}$	$\Delta t/\tau_{dep}$
fiducial	8.1%	1.3	4.2%	1.1
DEP0p5	3.9%	1.4	1.5%	1.4
DEP2	7.2%	1.7	3.6%	1.2
TDL5	8.9%	1.6	4.2%	1.2
EJ0p1	6.6%	1.3	3.9%	1.2
ST	8.0%	1.8	4.2%	1.5
STR	5.7%	1.8	3.1%	1.8

^aTotal chondrule formation probability $P_{c,tot}$ and the age spread of chondrules Δt normalized by the disk depletion time τ_{dep} for WL2019 and MRN planetesimal size distribution. Δt is defined as the time interval within which 70% of chondrules are formed (see also Figure 7).

tion probability $P_{c,tot}$ is about twice higher in the case of WL2019 size distribution compared to the MRN size distribution. This is because there is a larger number of smaller planetesimals in the “weakly coupled” group of $r_p \sim 50 - 2000$ km for the WL2019 size distribution (see Figure 4). For a given total mass of planetesimals, smaller planetesimals have a larger surface area, and P_c is proportional to the surface area that the planetesimals’ bow shocks sweep through. Indeed, we find that the total surface area of planetesimals from the WL2019 size distribution is about twice that from the MRN size distribution.

The contribution to the total chondrule formation probability P_c made by planetesimals of different sizes and at different times in the fiducial model is plotted in Figure 7. The total stacked histograms show the distribution of P_c as a function of planetesimal size. The contributions to P_c by planetesimals from different initial semi-major axis bins are indicated by different colors. It is evident that planetesimals with sizes $\sim 50 - 1000$ km are the main contributors to chondrule formation. The WL2019 size distribution does not have planetesimals with $r_p \gtrsim 1000$ km, but in the case of the MRN size distribution, $1000 - 2000$ km planetesimals also contribute to chondrule formation. This is expected, as the $\sim 50 - 2000$ km planetesimals are in the “weakly coupled” group that can be excited to large eccentricities.

Overall, chondrule formation are dominated by planetesimals with initial semi-major axis $1.5 \text{ AU} \lesssim a_{p,0} \lesssim 2.5 \text{ AU}$. Because the Keplerian velocity is smaller further away from the Sun, it is difficult for planetesimals with $a_{p,0} \gtrsim 2.5 \text{ AU}$ to gain high enough velocities for chondrule formation. This can be seen in the distribution of P_c with relative velocity in the left panel of Figure 8. Planetesimals with $a_{p,0} \lesssim 1.5 \text{ AU}$ do not contribute significantly to chondrule formation, because it is less likely for their orbits to cross the asteroid region of $1.5 - 3.0 \text{ AU}$, where we assume chondrules are formed. In principle, chondrules can form inside 1.5 AU and be transported outward to the asteroid belt region today, but this scenario is beyond the scope of this paper.

Generally speaking from Figure 8, most chondrules form in shocks of very high velocities $v_{rel} \approx 12 - 18 \text{ km/s}$, in low density gas $\rho_g \approx 10^{-11.5} - 10^{-10.5} \text{ g/cm}^3$ when the disk is significantly depleted relative to the MMSN, and in the inner asteroid belt region $R \lesssim 2.5 \text{ AU}$.

Mean motion resonance, on the other hand, does not cause a significant amount of chondrule heating. Al-

though the planetesimals close to the 2:1 resonance with Jupiter can be excited to eccentricities $e_p > 0.5$, they contribute very little to chondrule heating (Figure 7). This is because the 2:1 resonance is in the outer region of the disk where the Keplerian velocity is relatively low, and v_{rel} is hardly ever large enough for chondrule formation. This is consistent with the result in Nagasawa et al. (2014).

3.3.2. Dependence on Model Parameters

Table 2 shows that the total chondrule formation probability $P_{c,tot} \approx 4 - 9\%$, only varies by a factor of ~ 2 for a wide range of model parameters. In this section, we discuss the reasons why $P_{c,tot}$ is relatively insensitive to these parameters.

Doubling the disk depletion timescale to $\tau_{dep} = 2 \text{ Myr}$ (model DEP2) does not have a significant effect on the chondrule formation probability. This is because both the location of ν_5 and the disk mass only depend on t/τ_{dep} . A planetesimal with initial semi-major axis $a_{p,0}$ encounters ν_5 at a certain value of t/τ_{dep} and a corresponding disk mass, independent of τ_{dep} (Figure 2). Therefore, the eccentricity excitation and damping rates of the planetesimal are largely unchanged. If τ_{dep} is too short, however, ν_5 migrates in so rapidly that the planetesimals do not have enough time to react to the ν_5 resonance before it passes through, leading to less efficient eccentricity excitation. This is why $P_{c,tot}$ in model DEP0p5 is reduced.

Moreover, $P_{c,tot}$ is rather insensitive to the initial eccentricity of Jupiter (model EJ0p1) and the tidal damping timescale (model TDL5). The planetesimal’s eccentricity excitation rate is proportional to e_J (Equation 4), and its eccentricity tidal damping rate is inversely proportional to τ_{tidal} (Equation (28)). However, the chondrule formation probability is not sensitive to the eccentricity excitation and damping rates, as long as the planetesimal can gain high enough eccentricity to cause chondrule formation. When the eccentricity of the planetesimal is higher, although the chondrule formation rate is higher, the planetesimal also migrates inward faster and thus spends less time in the asteroid belt region. These two effects roughly cancel each other, and the resulting $P_{c,tot}$ is largely unchanged.

Introducing Saturn does not have a strong effect on $P_{c,tot}$ either (models ST and STR). The sweeping secular resonance by Saturn occurs at a later time than that by Jupiter. As most planetesimals in the “weakly damping” group move inward rapidly when they encounter the Jovian secular resonance and gain high eccentricities, they do not encounter the secular resonance by Saturn most of the time. Saturn modulates the eccentricity of Jupiter, changing the eccentricity excitation rate of the planetesimals. Saturn’s gravity and the larger gap size also change the precession rate of Jupiter, and cause the ν_5 resonance to occur at a slightly different time when the disk mass is different, changing the eccentricity damping rate of planetesimals. However, $P_{c,tot}$ is relatively insensitive to the eccentricity excitation rate and damping rate for the reasons stated in the previous paragraph.

3.3.3. Comparison to Observations

Can the chondrule formation probability in our model explain the fraction of chondrules in our current aster-

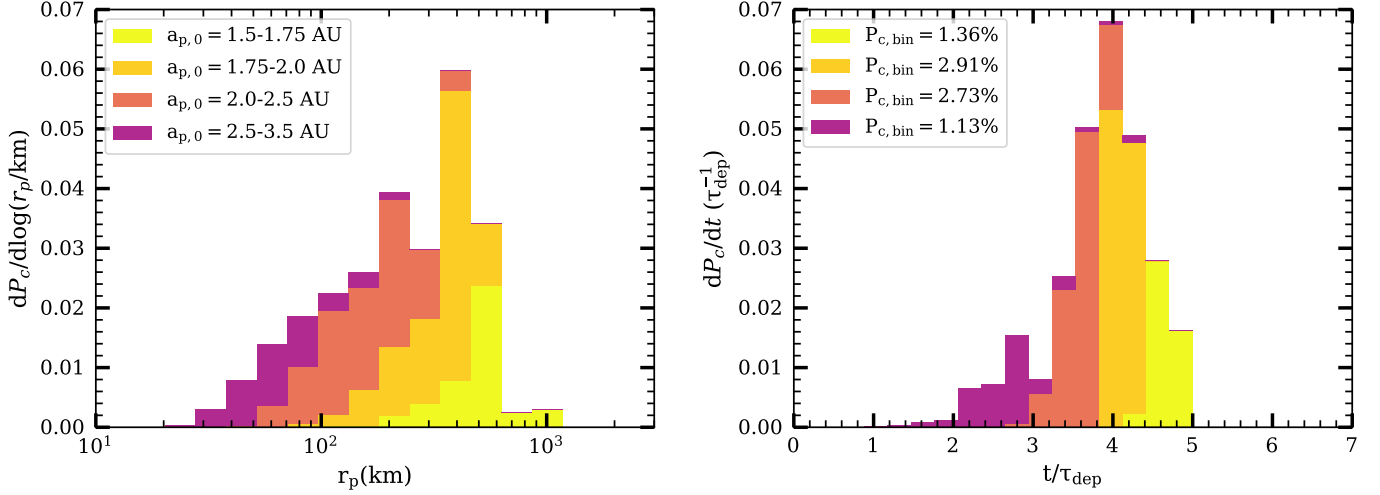


Figure 7. Stacked histograms of the chondrule formation probability in the fiducial model. *Left panel:* The contribution to the total chondrule formation probability P_c made by planetesimals of different sizes at each initial semi-major axes bin (see figure legends). The planetesimals are assumed to have a surface density of 1% of the initial gas disk mass, and a size distribution from simulations by WL2019 (see Figure 4 and discussions). *Right panel:* Similar to the left panel, but for the contribution to P_c at different times. The total chondrule formation probability in each $a_{p,0}$ bin, $P_{c,\text{bin}}$, is marked in the figure legends.

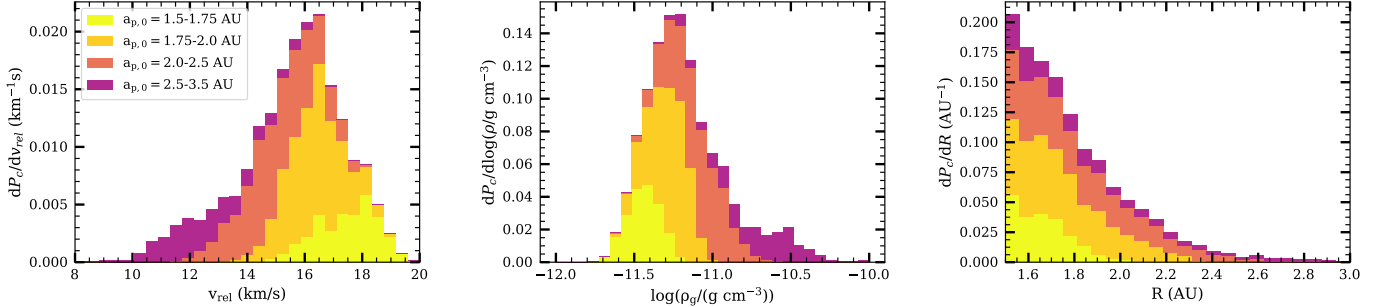


Figure 8. Similar to the right panel of Figure 7, but for the contribution to P_c by planetesimals with different relative velocities with respect to the gas (*left*), and by chondrule heating events with different local gas densities (*middle*) and distances from the Sun (*right*).

oid belt? From meteorite samples found on Earth, ordinary chondrites are the most commonly found type of meteorites (Sears & Dodd 1988). Chondrules make up 60 – 80% of the volume of ordinary chondrites, and a rough estimate gives that $\sim 10\%$ of the present day asteroid belt can be made of chondrules (Desch et al. 2005). However, there are also arguments that chondrules may be much rarer than commonly believed. Sears (1998) pointed out two main sources of bias: First, ordinary chondrites are much more robust than volatile-rich carbonaceous chondrites, and thus much more likely to survive falling through the Earth’s atmosphere. Second, the meteorites that fall on Earth may not be a fair sample of the asteroid belt. He estimated that after the correction of biases, ordinary chondrites make up less than 4% of the asteroid belt. Meibom & Clark (1999) argues that the sample of extraterrestrial dust particles is much less biased, and less than $\sim 1\%$ of them have a composition similar to ordinary chondrites. In general, our simulated chondrule formation probability of 4 – 9% is consistent with these observational constraints.

4. DISCUSSION

4.1. The Depletion Timescale of the Solar Nebula

Assuming the ages of chondrules measured from radioactive isotopes indicate the time that they went

through flash-heating, the age spread of chondrules can be indicative of the disk depletion timescale, as shown in Table 2 and discussed in Section 3.3.1.

Isotopic measurement of chondrules’ ages indicate that chondrule formation started 0.7 Myr after the formation of CAIs, and lasted for at least 2.4 Myr and potentially up to 5 Myr, with most chondrules formed 1 – 3 Myr after the CAIs (see reviews by Connolly et al. 2006; Scott 2007). This is consistent with a disk depletion time of $\tau_{\text{dep}} \approx 1$ Myr. This is also broadly consistent with the observations of young stellar clusters, which suggest that about half of the young stars lose their disk in $\sim 1\text{--}3$ Myr (Haisch et al. 2001; Armitage et al. 2003; Ribas et al. 2015; Richert et al. 2018).

We note that $t = 0$ in Figures 7 does not indicate the time of CAI formation. It corresponds to the time when the disk mass equals the MMSN mass, which is chosen to be the initial condition of our models (see also Figure 1). CAI formation can occur either before or after $t = 0$ in our models. Moreover, the relevant timescale for chondrule formation is measured by the migration timescale of ν_5 , or τ_{dep} , which does not necessarily correspond to a physical time. There is no reason why τ_{dep} in Equation (7) has to remain constant throughout the disk evolution. Gap formation may actually lead to an accumulation of disk gas in the region outside Jupiter’s orbit while the in-

ner disk may deplete rapidly. Photoevaporation may also accelerate the pace of surface density decline in the inner disk region. However, the conclusion that the age spread of chondrules is comparable to the time that ν_5 sweeps through the asteroid belt region is unchanged even if τ_{dep} varies with time.

4.2. The Formation of Jupiter

In our model, the formation of Jupiter is essential for chondrule heating. However, unlike the model of chondrule heating by mean motion resonance (Weidenschilling et al. 1998), the onset of chondrule heating and Jupiter’s formation do not have to be coeval. The only constraint on the formation time of Jupiter is that it has to be before the formation of chondrules, not more than 0.7 Myr after the CAIs formed. The timing of chondrule formation indicates when the ν_5 resonance passes through the asteroid belt, which is directly tied to a disk mass of 1 – 10% of the MMSN. A recent study by Kruijer et al. (2017) suggests that the composition of different types of meteorites indicates that Jupiter formed and opened a gap in the disk within 1 Myr after the formation of the CAIs.

Given that Jupiter is likely to form in the gas-rich disk before the formation of chondrules, the sweeping secular resonance seems to be hardly avoidable: as long as the gas disk is more than $\sim 10\%$ of the MMSN after the formation of Jupiter, the ν_5 resonance will pass through the asteroid belt region and excite the eccentricities of any large planetesimals that may be there. There is indeed evidence that large planetesimals were present before chondrule formation: iron meteorites, which come from the fragments of cores of the earliest-formed differentiated planetesimals, are dated to be accreted as early as 0.1 – 0.3 Myr after the formation of CAIs (Kruijer et al. 2014, 2017).

In addition, the formation of Jupiter can lead to relocation of nearby planetesimals through scattering (Zhou & Lin 2007). The subsequent propagation of Jupiter’s sweeping secular resonance can lead to collisional fragmentation, merger, and effective clearing of the main belt region (Nagasawa et al. 2005; Thommes et al. 2008; Zheng et al. submitted).

5. SUMMARY

In this paper, we propose that chondrules can form efficiently when the Jovian sweeping secular resonance passes through the asteroid belt region and excites the eccentricities of planetesimals in the early solar protoplanetary disk. We use semi-analytic models and numerical simulations to study the orbital evolution of planetesimals and its effect on chondrule formation. Our main findings are summarized as follows.

1. Planetesimals with sizes $\sim 50 - 2000$ km are subject to relatively weak gas drag in the disk. They can be excited to eccentricities $e_p > 0.6$ by the Jovian sweeping secular resonance in the asteroid belt region and cause chondrule formation. Smaller or bigger planetesimals suffer from either strong eccentricity damping or rapid inward migration by the gas drag, and thus cannot gain high enough eccentricities required for chondrule heating (Figure 6).

2. Most chondrules form in high velocity shocks $v_{\text{rel}} \approx 12 - 18$ km/s, in low density gas $\rho_g \approx 10^{-11.5} - 10^{-10.5}$ g/cm³ when the disk is depleted to 1 – 10% of the mass of the MMSN, and in the inner asteroid belt region $R \lesssim 2.5$ AU (Figure 8).
3. The average chondrule formation probability between 1.5 – 3.0 AU is about 4 – 9%, consistent with observational constraints (Table 2).
4. Our model suggests that the depletion timescale for the protoplanetary disk around the Sun is comparable to the age spread of chondrules at $\tau_{\text{dep}} \approx 1$ Myr (Table 2), and that Jupiter must have formed before the formation of chondrules, not more than 0.7 Myr after the CAIs.

6. ACKNOWLEDGEMENT

M. Gong thanks the support from the Max Planck Institute for extraterrestrial Physics and Princeton University. X. Zheng is supported by the China Postdoctoral Science Foundation (Grant No. 2017M610865). D.N.C. Lin thanks IAS Princeton, IAS Tsinghua, IoA Cambridge, and ITC Harvard for support when this work was completed. This work is partly supported by the National Key Basic Research and Development Program of China (No. 2018YFA0404501 to SM) and by the National Science Foundation of China (Grant No. 11333003, 11390372 and 11761131004 to S. Mao). We also thank the anonymous referee for a helpful report.

REFERENCES

- Aarseth, S. J. 2003, *Gravitational N-Body Simulations*, 430
 Adachi, I., Hayashi, C., & Nakazawa, K. 1976, *Progress of Theoretical Physics*, 56, 1756
 Armitage, P. J., Clarke, C. J., & Palla, F. 2003, *MNRAS*, 342, 1139
 Artymowicz, P. 1993, *ApJ*, 419, 166
 Baruteau, C., Crida, A., Paardekooper, S.-J., et al. 2014, *Protostars and Planets VI*, 667
 Bryden, G., Chen, X., Lin, D. N. C., Nelson, R. P., & Papaloizou, J. C. B. 1999, *ApJ*, 514, 344
 Ciesla, F. J., & Hood, L. L. 2002, *Icarus*, 158, 281
 Connolly, Jr., H. C., Desch, S. J., Ash, R. D., & Jones, R. H. 2006, *Transient Heating Events in the Protoplanetary Nebula*, ed. D. S. Lauretta & H. Y. McSween, 383–397
 Desch, S. J., Ciesla, F. J., Hood, L. L., & Nakamoto, T. 2005, in *Astronomical Society of the Pacific Conference Series*, Vol. 341, *Chondrites and the Protoplanetary Disk*, ed. A. N. Krot, E. R. D. Scott, & B. Reipurth, 849
 Desch, S. J., Morris, M. A., Connolly, H. C., & Boss, A. P. 2012, *Meteoritics and Planetary Science*, 47, 1139
 Dobbs-Dixon, I., Li, S. L., & Lin, D. N. C. 2007, *ApJ*, 660, 791
 Dullemond, C. P., Stammer, S. M., & Johansen, A. 2014, *ApJ*, 794, 91
 Dürmann, C., & Kley, W. 2015, *A&A*, 574, A52
 Epstein, P. S. 1924, *Phys. Rev.*, 23, 710
 Fendyke, S. M., & Nelson, R. P. 2014, *MNRAS*, 437, 96
 Haisch, Jr., K. E., Lada, E. A., & Lada, C. J. 2001, *ApJ*, 553, L153
 Hayashi, C. 1981, *Progress of Theoretical Physics Supplement*, 70, 35
 Iida, A., Nakamoto, T., Susa, H., & Nakagawa, Y. 2001, *Icarus*, 153, 430
 Kominami, J., & Ida, S. 2002, *Icarus*, 157, 43
 Kruijer, T. S., Burkhardt, C., Budde, G., & Kleine, T. 2017, *Proceedings of the National Academy of Science*, 114, 6712
 Kruijer, T. S., Touboul, M., Fischer-Gödde, M., et al. 2014, *Science*, 344, 1150
 Mann, C. R., Boley, A. C., & Morris, M. A. 2016, *ApJ*, 818, 103

- Mathis, J. S., Rumpl, W., & Nordsieck, K. H. 1977, *ApJ*, 217, 425
- Meibom, A., & Clark, B. E. 1999, *Meteoritics and Planetary Science*, 34, 7
- Morris, M. A., Boley, A. C., Desch, S. J., & Athanassiadou, T. 2012, *ApJ*, 752, 27
- Murray, C. D., & Dermott, S. F. 1999, *Solar system dynamics*
- Muto, T., Takeuchi, T., & Ida, S. 2011, *ApJ*, 737, 37
- Nagasawa, M., Lin, D. N. C., & Ida, S. 2003, *ApJ*, 586, 1374
- Nagasawa, M., Lin, D. N. C., & Thommes, E. 2005, *ApJ*, 635, 578
- Nagasawa, M., Tanaka, K. K., Tanaka, H., et al. 2014, *ApJ*, 794, L7
- Paardekooper, S.-J., Baruteau, C., & Kley, W. 2011, *MNRAS*, 410, 293
- Papaloizou, J. C. B., & Larwood, J. D. 2000, *MNRAS*, 315, 823
- Ribas, Á., Bouy, H., & Merín, B. 2015, *A&A*, 576, A52
- Richert, A. J. W., Getman, K. V., Feigelson, E. D., et al. 2018, *MNRAS*, 477, 5191
- Scott, E. R. D. 2007, *Annual Review of Earth and Planetary Sciences*, 35, 577
- Sears, D. W. G. 1998, *ApJ*, 498, 773
- Sears, D. W. G., & Dodd, R. T. 1988, *Overview and classification of meteorites*, ed. J. F. Kerridge & M. S. Matthews, 3–31
- Shakura, N. I., & Sunyaev, R. A. 1973, *A&A*, 24, 337
- Shu, F. H., Shang, H., Gounelle, M., Glassgold, A. E., & Lee, T. 2001, *ApJ*, 548, 1029
- Thommes, E., Nagasawa, M., & Lin, D. N. C. 2008, *ApJ*, 676, 728
- Urey, H. C., & Craig, H. 1953, *Geochim. Cosmochim. Acta*, 4, 36
- Walsh, K. J., & Levison, H. F. 2019, *Icarus*, 329, 88
- Ward, W. R. 1981, *Icarus*, 47, 234
- . 1988, *Icarus*, 73, 330
- Ward, W. R., Colombo, G., & Franklin, F. A. 1976, *Icarus*, 28, 441
- Weidenschilling, S. J., Marzari, F., & Hood, L. L. 1998, *Science*, 279, 681
- Whipple, F. L. 1972, in *From Plasma to Planet*, ed. A. Elvius, 211
- Xu, Z., Bai, X.-N., & Murray-Clay, R. A. 2017, *ApJ*, 847, 52
- Zheng, X., Lin, D. N. C., & Kouwenhoven, M. B. N. 2017, *ApJ*, 836, 207
- Zheng, X., Lin, D. N. C., Mao, S., et al. submitted
- Zhou, J.-L., & Lin, D. N. C. 2007, *ApJ*, 666, 447
- Zuckerman, B., Forveille, T., & Kastner, J. H. 1995, *Nature*, 373, 494